2022-05-01

Ultrahigh Strength-High Ductility Combination Low Density Austenitic Steel: Effect Of Aging Temperature And Strain Rate

Jaehyun Kim
The University of Texas at El Paso

Recommended Citation

Kim, Jaehyun, "Ultrahigh Strength-High Ductility Combination Low Density Austenitic Steel: Effect Of Aging Temperature And Strain Rate" (2022). *Open Access Theses & Dissertations*. 3507.
https://scholarworks.utep.edu/open_etd/3507

ULTRAHIGH STRENGTH-HIGH DUCTILITY COMBINATION LOW DENSITY AUSTENITIC STEEL: EFFECT OF AGING TEMPERATURE AND STRAIN RATE

JAEHYUN KIM

Master's Program in Metallurgical and Materials Engineering

APPROVED:

R. Devesh K. Misra, Ph.D., Chair

Srinivasa Rao Singamaneni, Ph.D.

Guikuan Yue, Ph.D.

Stephen L. Crites, Jr., Ph.D.
Dean of the Graduate School

ULTRAHIGH STRENGTH-HIGH DUCTILITY COMBINATION LOW DENSITY AUSTENITIC STEEL: EFFECT OF AGING TEMPERATURE AND STRAIN RATE

by

JAEHYUN KIM

THESIS

Presented to the Faculty of the Graduate School of
The University of Texas at El Paso
in Partial Fulfillment
of the Requirements
for the Degree of

MASTER OF SCIENCE

Department of Metallurgical, Materials and Biomedical Engineering
THE UNIVERSITY OF TEXAS AT EL PASO
May 2022

ACKNOWLEDGEMENTS

I would like to express my heartfelt gratitude to the internationally renowned professor and my research advisor, Dr. R. Devesh K. Misra for giving me the opportunity to work with him. His constant support, guidance and encouragement filled me with enthusiasm throughout my master's research. His countless valuable opinion, help and guidance were very important in significantly increasing the intellectual merit of the master's research.

Special thanks to Dr. Srinivasa Rao Singamaneni and Dr. Guikuan Yue for serving as members of the thesis committee. I would like to thank the Department of Metallurgical, Materials, and Biomedical Engineering for their support.

I sincerely thank my parents for their unconditional support. Finally, I want to take this opportunity to thank all my relatives and friends who contributed directly or indirectly in the successful completion of thesis.

ABSTRACT

The objective of the study was to optimize the post-thermal treatment of hot rolled Fe-0.92C-26.3Mn-8.79Al-0.05Nb steel. In this regard, the hardness of the experimental steel was studied as a function of aging time and/or strain rate. The study provided an understanding of aging heat treatment for the experimental steel, which was processed by vacuum induction melting, followed by thermo-mechanical rolling involving multiple passes. The rolled steel was subsequently annealed at 900 °C for 4 h followed by water quenching. X-ray diffraction in scanning mode of $2\theta=20\text{-}100^{o}$ indicated the presence of austenite structure. In order to study the influence of aging at 550 °C for 20 h, mechanical properties (yield strength, ultimate tensile strength, and elongation) were determined via tensile tests and compared with as-rolled and solution treated at 950 °C for 1, followed by quenching. Additionally, to study the effect of aging for different times (1, 10, 25, 50, 75 h) at 500 °C, Vickers hardness measurements indicated increase of hardness with aging time, and there was a different of ~138 HV1 between 1 h and 75 h aged samples. Scanning electron microscopy was used to study microstructural variation on 1 h and 75 h aged samples. The size of annealing twins for each aging time was measured using Image J software. Lastly, the effect of strain rate on hardness values was studied. The study enabled the optimization of post-thermal treatment on Fe-Mn-Al-C-Nb low-density steel.

TABLE OF CONTENTS

LIST OF TABLES

LIST OF FIGURES

CHAPTER 1: INTRODUCTION

Due to ever tighter safety standards and environmental regulations, mobility industry has been pursued long time to manufacture vehicles from low-density steels that have high strength and ductility. Fe-Mn-Al-C quaternary alloy has been considered a strong potential to be used due to high specific strength and ductility based on various hardening mechanisms such as κ-carbide precipitation, dislocation slip, and twins controlled by alloying elements, strain rate, and heat treatment.

Fe-Mn-Al-C quaternary alloy is known to show at least five phases in the equilibrium state. Those include γ-austenite, α-ferrite, κ-carbide, M3C carbide and β-Mn. When it comes to matrix phases, they would be γ-austenite, α-ferrite, and the duplex of γ-austenite and α-ferrite.

The excellent mechanical strength of Fe-Mn-Al-C alloy derives from κ-carbides, L'12 ordered FCC carbides of $(Fe, Mn)_3AlC$. Although there is no clear theory to explain κ-carbides formation, some studies reported the formation mechanism of κ-carbides. Spinodal decomposition has been considered a dominant theory which involves nucleation of κ-carbides by the chemical partitioning of Al and C contents during the reaction [1]. Another theory demonstrated with γ-based Fe-20Mn-9Al-3Cr-1.2C alloy [2] explained that κ-carbides go through typical nucleation and growth on the basis of no chemical partitioning and a positive Gribbs energy curvature at temperatures of 400-800 °C. Another study [3, 32] also suggested κ-carbides precipitation through typical eutectoid reaction ($\gamma \rightarrow \alpha+\kappa$) where γ-austenite is decomposed into the lamellae of α-ferrite and κ-carbide within γ-grain boundaries so that γ-austenite disintegrates into α-ferrite and needle-like κ-carbide [4].

It effectively pins dislocation movements so that causes the transition of dislocation type from edge to screw dislocation that has line vector parallel to the Burgers vector [5]. Because severely bend dislocations by pinning are easy to cross-slip into other slip planes. The establishment of complex slip system eventually leads to the decline in dislocation mean free path [5, 6]. Accordingly, precipitation hardenability of κ-carbide significantly depends on the interfacial coherency between matrix and κ-carbide and the location of κ-carbide.

γ-austenite and κ-carbide have been reported to have similar lattice orientation with 3% lattice misfit in [100]κ//[100]γ and [010]κ//[010]γ [7-10], whereas α-ferrite and κ-carbide exhibit 6% lattice misfit resulting in semi-coherency [11, 12]. So, γ-austenite is chosen as the matrix phase to maximize the precipitation strengthening from κ-carbides.

The location of κ-carbide precipitation also importantly affect mechanical the mechanical properties of Fe-Mn-Al-C alloys. There exists inter- and intra-granular κ-carbides in microstructure, and κ-carbides grow to elongated rod-like shape when they get coarser [11, 13]. While inter-granular κ-carbides make the alloys brittle working as the paths for crack initiation and propagation [14] as opposed to the softer γ-matrix containing intra-granular κ-carbides [15].

1.1.STRAIN HARDENING IN AUSTENITIC LOW-DENSITY ALLOY

Besides κ-carbides precipitation, Fe-Mn-Al-C alloys feature great strain hardenability from the different stages of dominant deformation mechanism. This study will mainly deal with the strain hardening in γ-based alloys because γ-austenite is the matrix phase of the experimental steel. low-density steel. Strain hardening mechanisms are generally divided into transformation-induced plasticity (TRIP), twinning-induced plasticity (TWIP), and microband-induced plasticity (MBIP).

TRIP is the strain hardening mechanism shown from Fe-Mn-Al-C with stacking fault energy (SFE) less than 20 mJ m^{-2} whereas TWIP appears to be a dominant hardening mechanism with SFE of 20-40 mJ m^{-2} [16]. Pierce et al. [17] exhibited the relationship between SFE and change in deformation mechanisms. In the reference, the change in chemical composition from Fe-22Mn-3Al-3Si to Fe-25Mn-3Al-3Si led to the increase in SFE from 15 mJ m^{-2} to 21 mJ m^{-2}. This showed TRIP at 15 mJ m^{-2} changed to TWIP at 21 mJ m^{-2}. Grässel et al. [18] found from Fe-(15-30)Mn-(2-4)Si-(2-4)Al alloys that incremental Mn content changes deformation mechanism from TRIP to TWIP as well. With more Mn content, mechanical properties of alloys got influenced showing the decrease in ultimate tensile strength (UTS) from 1100 to ≈ 600 MPa and the increase in total elongation (e_t) from 40 to about 90%. Based on Fe-3Si-3Al-(15-25)Mn alloys, a similar study specified the relationship between Mn content, SFE, and deformation mechanism [19]. TRIP occurred with Mn contents of 15-20 wt.% Mn, but TRIP was replaced with TWIP when Mn content reached to 22 wt.%. Hence it is noted that the alloying elements results in different deformation mechanisms through the variation of SFE value.

MBIP dominates strain hardening mechanism when the SFE becomes higher than ≈ 60 mJ m^{-2} [20]. In general knowledge for FCC materials with low SFE, dislocation movement limited on a single slip plane because of not enough three-dimensional mobility for cell formation [21]. On the other hand, wavy dislocation glides and the evolution of dislocation cells are observed in FCC materials with high SFE due to frequent dislocation cross-slip during strain [22]. However, the general tendency is not applicable to low-density alloys as planar dislocation glides are found to be dominant in the alloys with the SFE higher than ≈ 60 mJ m^{-2} [20, 23]. The microbands formation in the alloys with SFE higher than ≈ 60 mJ m-^{2} can be explained with Taylor lattices. Unlike wavy dislocation glides end up being dislocation cells, planar dislocation glides form Taylor lattices. During planar dislocation glides, crystallographic domain boundaries are formed between Taylor lattices, homogeneously organized dislocations with alternating planar order on their glide planes. The regions located between parallel domain boundaries are called microbands [24]. When a γ-based alloy with high SFE is deformed to a large extent, Taylor lattice rotates forming greater number of microbands. This narrows the interspacing distance between each microband and makes microbands intersected to one another, thus leading to Hall-Petch effect by grain subdivision intersected by microbands [25, 26].

For instance, Park et al. [27] traced the microstructural evolution of Fe-22Mn-0.6C and Fe-22Mn-6Al-0.6C alloys until fracture. Fe-22Mn-0.6C alloy with 21.5 mJ m^{-2} SFE presented highly packed mechanical twins and secondary twins over 20%. On the other hand, Fe-22Mn-6Al-0.6C alloy with 50.7 mJ m^{-2} SFE featured intersected microbands. Ma et al. [28] provided empirical confirmation for previously explained microbands formation by checking microstructural evolution along with different strains in Fe-28Mn-10Al-C-0.5Nb alloy with 84 mJ m^{-2} SFE. At 10% strain, Taylor lattice structure was observed. Microbands were recognized distinctively when the sample was strained over 25%. The space between microbands was reduced with further strain. Yoo et al. [26] demonstrated the strengthening effect of MBIP in comparison with TRIP and TWIP. The tensile test on Fe-28Mn-9Al-0.8C alloy with 85 mJ m^{-2} SFE obtained UTS of 843 MPa and e_t of 100%. The product of UTS and e_t was calculated to be 84,300 MPa% which is remarkably higher value than ~15,000 and 20,000 MPa% from TRIP and TWIP low-density steel.

1.2 THE INFLUENCE OF ALLOYING ELEMENTS (Mn, Al, C) ON STRAIN MECHANISM OF AUSTENITIC LOW-DENSITY ALLOY

As seen from previous references, there exists relationship between chemical composition, SFE, and deformation mechanism. That is, alloying elements can be used to control dominant deformation mechanism. Manganese (Mn) takes the highest weight percent among alloying elements and is known to increase SFE. Figure 1 [29] shows a parabolic graph of SFE values as a function of Mn content. In Figure 1, it can be identified that Mn increases SFE values from 15 ± 3 to 39 ± 5 mJ m^{-2}. Other work [30] also reported a linear relationship between SFE and Mn content. But both studies mean the same effect of Mn on SFE in that the SFE changed along with the amount of Mn.

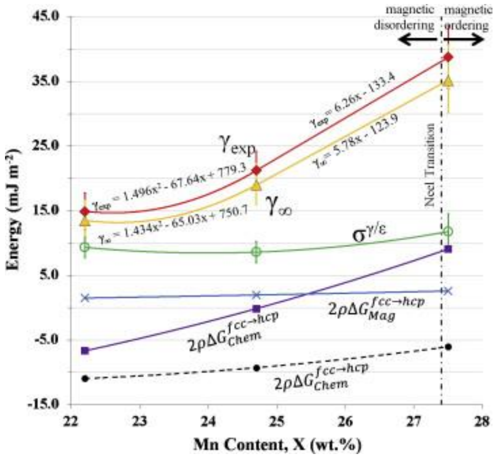

Figure 1: Experimental SFEs (γ_{exp}) as a function of Mn content in Fe–*X*Mn–2.7Al–2.9Si wt.% [29]

Because of effective density reduction by Al, 1.3% density reduction per 1 wt.% Al, Al is an important alloy element in the fabrication of low-density steel. [31-33]. To understand the influence of Al on constituent phase and deformation mechanism, there have been some studies on determining relationship between SFE and Al content. X-ray diffraction on Fe-22Mn-0.9C-(0/3/8)Al steel did show no phase transition from γ-austenite [34]. However, SFE values corresponded to 17.53 ± 2.47, 25.61 ± 4.76 and 50.76 ± 6.73 for 0, 3, and 8 wt.% Al contents, respectively. Those increase in SFE caused clear changes in deformation mechanisms. 0 and 3 wt.% Al deformed by combined deformations of TRIP and TWIP. By contrary, MBIP appeared to be the dominant in the steel containing 8 wt.% Al. As shown in Figure 2, the similar trend between SFE and Al content theoretically calculated through longitudinal spin fluctuation model and spin fluctuation calculations [35] demonstrates increasing linear SFE lines from Fe-18/22Mn-XAl-0.6C. On the other hand, the same theoretical calculations for Si contents resulted in the reduction of SFE values as a function of Si contents in Fe-18/31Mn-XSi-0.6/0.77C. Thermochemical modelling with alloying elements for Fe-22Mn-0.6C alloy in Figure 4 also indicates that the influence of Al and Si contents on SFE matches with the previous studies above [36-38]. But, in the case of Si addition, SFE increased until 4 wt.% and then showed its reduction after that as shown in Figure 3.

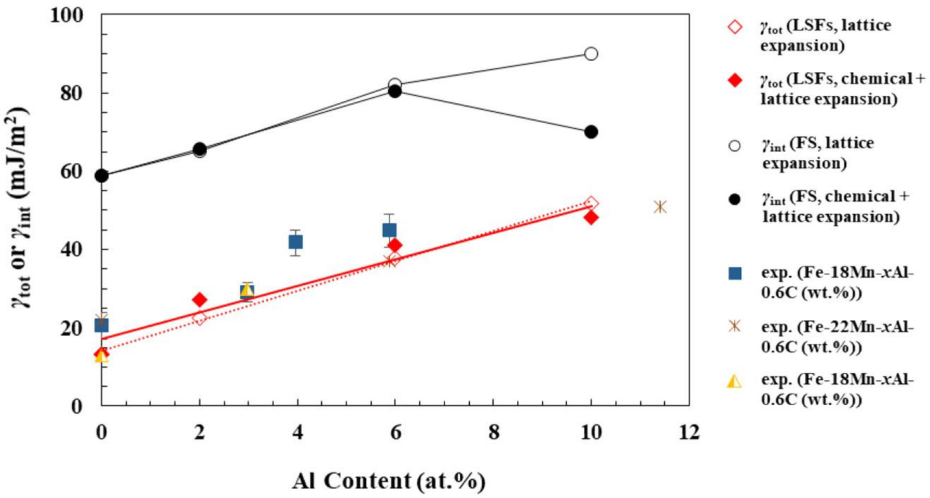

Figure 2: The effect on Al content on SFE (γ_{tot}) expected by LSF and FS [35]

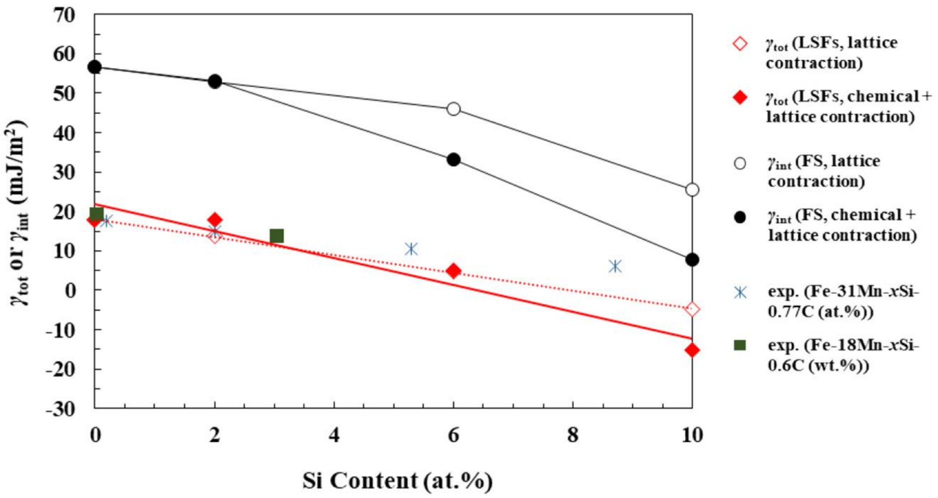

Figure 3: The effect of Si content on SFE (γ_{tot}) expected by LSF and FS [35]

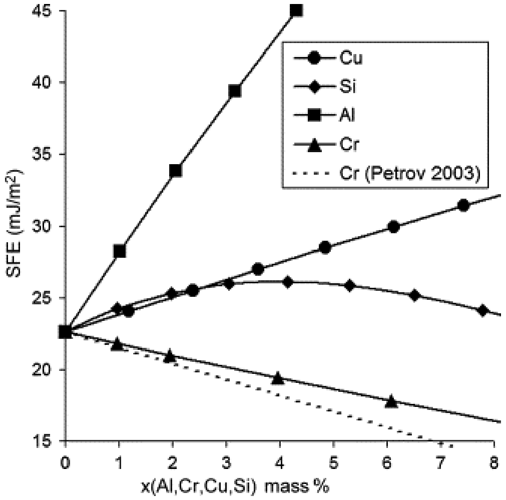

Figure 4: Thermochemical modelling prediction for the effect of alloying elements on the SFE of the Fe-22Mn-0.6C [36]

As mentioned above, SFE value is the factor to control deformation mechanism in low-density steel. So, the varied SFE values by Al contents are associated with mechanical properties and constituent phases.

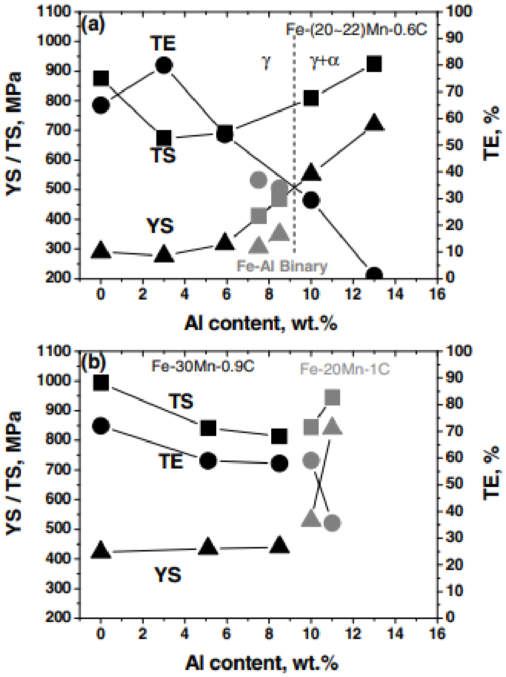

Figure 5: Tensile tests on Fe-Mn-Al-C alloy with different Al contents up to 13 wt.% [39]

Figure 5 (a) [39] compared tensile test results between Fe-(20-22)Mn-XAl-0.6C and Fe-XAl ferritic alloys in the addition of Al up to 13 wt.%. With more than 9 wt.% Al, there existed a phase transition from γ-austenite to the duplex phase of α-ferrite and γ-austenite. This means Al stabilizes α-ferrite in low-density steel. However, phase transition did make no shift to the mechanical behavior of Fe-(20-22)Mn-XAl-0.6C. Fe-(20-22)Mn-XAl -0.6C [39-41] and Fe-XAl ferritic alloys [39, 42] have same behavior of mechanical properties in Fig 5 (a) as the increased Al content resulted in the increment of strength and expense of total elongation. For the abrupt increase of UTS and decrease of e_t around 3 wt.% Al, it turned out to be due to the changed deformation mechanism from TWIP to MBIP. In Figure 5 (b), Fe-30Mn-0.9C-Al and Fe-20Mn-1.0C-Al alloys are composed γ-austenite for the whole range of Al content. This can be explained with high contents of Mn and C which prevent phase transition as γ-austenite stabilizers.

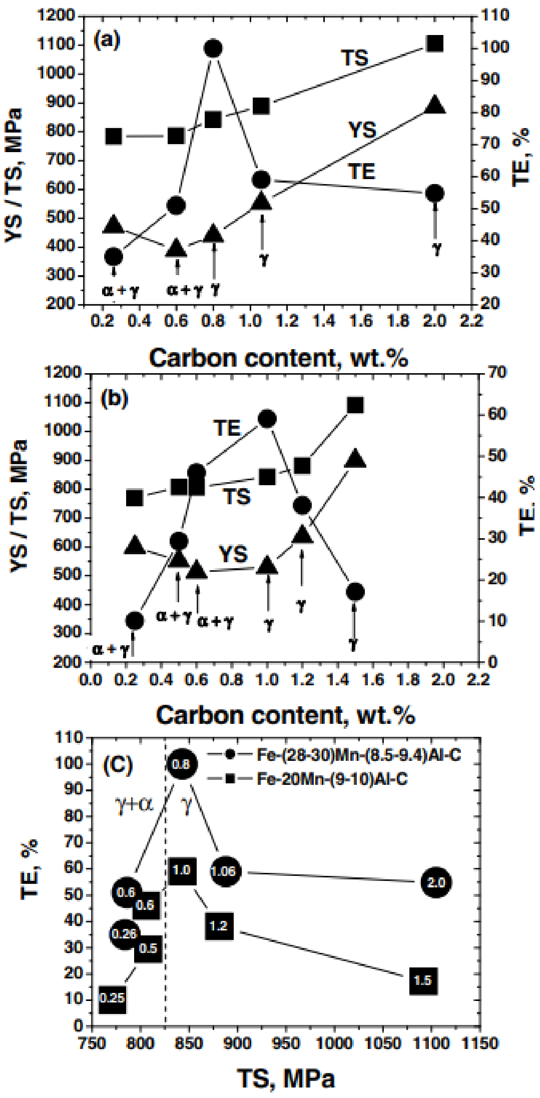

Figure 6: Effect of carbon content on the mechanical properties of Fe-Mn-Al-C alloys [39]

As seen in Figure 6 (a), increasing carbon content change the matrix phase from α-ferrite to γ-austenite. UTS and Yield strength (YS) proportionally increases with C contents regardless of constituent phases. By contrary, e_t in Fig 6 (a) and 6 (b) seems related to matrix phases based on rapid deterioration of ductility after austenite becomes matrix phase. This behavior originates from κ-carbides precipitation during solution treatment followed by quenching because once single γ-austenite becomes matrix phases, excessive carbon may facilitate κ-carbides precipitation inside grain and along the γ-austenite grain boundaries. upon quenching after solution treatment.

Fig 6 (c) rearranged UTS and e_t in Figure 6 (a) and 6 (b) to understand effect of Mn content in low-density steel with same Al contents. Compared to Fe-20Mn-(9-10)Al-C, Fe-(28-30)Mn-(8.5-9.4)Al-C alloys retain higher e_t at same UTS. Therefore, it is note that Mn content contributes to the better balance of strength and ductility.

1.3. AGEING EFFECT ON THE HARDNESS OF LOW-DENSITY STEEL

Making low-density alloys to have smaller thickness would be one of the simplest ways to the reduction of weight used for products. However, since stiffness shows an inverse relationship to thickness, achievement of weight reduction is not available with excessive reduction in thickness. Instead, solution treatment and age hardening are another approach compensating for the decreases of stiffness and hardness from thin thickness.

Fe-30Mn-9Al-1Si-1C-0.5Mo alloy was subjected to studying age hardenability as a function of aging time at 773 K after solution treat and quenching (STQ) in the range of 1173-1323 K [43]. The highest hardness of the alloy was observed from a sample that had STQ at 1173 K as lower STQ leads to a great number of nuclei, smaller grain size, and Hall-Petch strengthening. The sample with STQ at 1173 K appeared to have the largest volume fraction of κ-carbides among all the samples with STQ in the range of 1173-1323 K. Which was associated with high rate of age hardening shown in the sample with STQ at 1173 K. Aging at 773 K brought about hardness increase in most samples except whereas a sample with STQ at 1323 K did not respond to age hardening until 20 hours.

The relationship of peak hardness with κ-carbide volume fraction was studied by aging Fe-31.2Mn-7.5Al-1.3-Si-0.9C alloy, which has preexisting κ-carbides prior to aging due to homogenization and solubilization at 1050 °C, at aging temperatures of 500, 550, and 600 °C [44]. all samples reached the same peak hardness without respect to aging temperatures of 500, 550, and 600 °C. However, aging temperatures had their difference in that samples gained the peak hardness and entered into over-aging earlier at higher temperature.

Thermo-mechanical treatment (TMT), hot compression to a sample at deformation temperature, was compared to conventional aging treatment in Fe-20.71Mn-11.12Al-1.55C alloy [45]. For TMT, alloy samples were heated up to different temperatures of 900, 1000, and 1150 °C and hot-compressed by true strain, ε, of 0.7 at different strain rates of 10^{-2} s^{-1}, 10^{-1} s^{-1}, and 1 s^{-1}. Figure 7 shows Vickers microhardness of alloy samples that went through TMT at different deformation temperatures. Their hardness values are higher in comparison to the one without TMT but did not exhibit visible increase in hardness along with increasing temperatures. It was rather distinguishable that faster strain rate to alloy samples at the same temperature resulted in higher hardness.

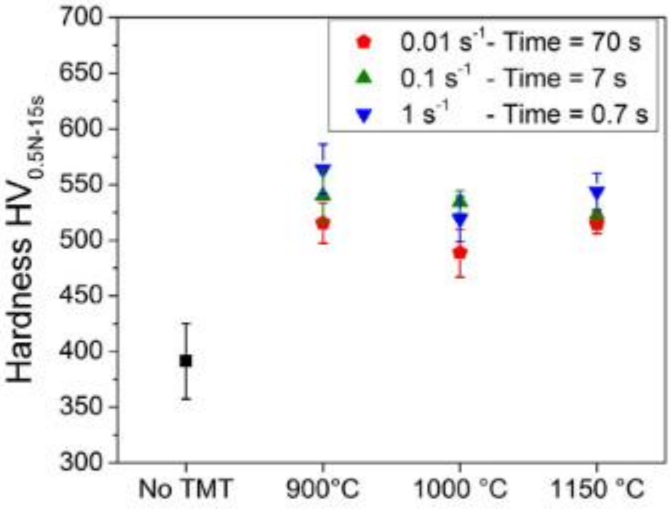

Figure 7: Vickers hardness of Fe-20.71Mn-11.12Al-1.55C alloy as function of TMTs at different deformation temperatures and strain rates [45]

Conventional aging up to 15 hours at 550 °C was carried out at the same alloy for comparative measure. As shown in Figure 8, the alloy sample arrived in the highest hardness with about 540 HV after 2 hours and then led to slight decreases under longer aging conditions. When comparing TMT with conventional aging, TMT achieved almost same Vickers hardness having cuboidal κ-carbides coarsening in microstructure such as Figure 9, which is generally found in aged Fe-Mn-Al-C alloys [46-49].

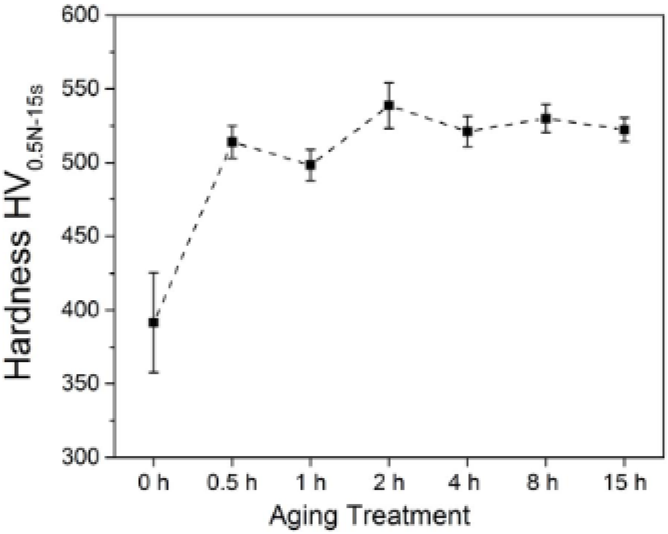

Figure 8: Vickers hardness of Fe-20.71Mn-11.12Al-1.55C alloy in conventional aging treatment [45]

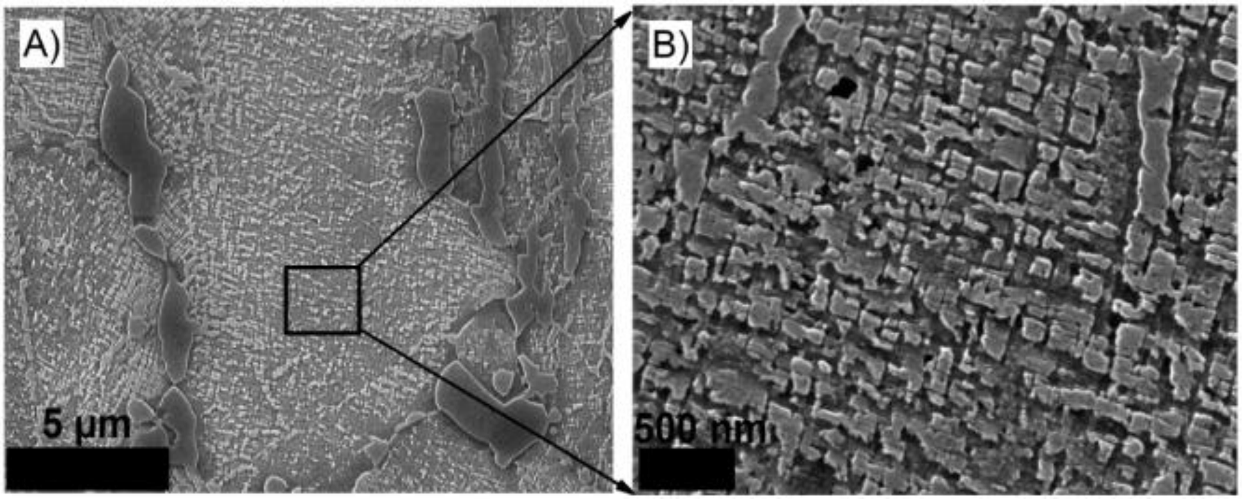

Figure 9: SEM of cuboidal κ-carbides after TMT at 1150°C & 10^{-1} s^{-1} [45]

In Figure 10, different relationship between hardness and age hardening was reported from aging Fe-18Mn-10Al-0.9C-5Ni steel at different temperatures such as 500, 530, 570, 600 °C [51]. As observed in the prior references [43, 44], aging temperature influenced proportionally to age hardening sensitivity. On the other hand, the peak hardness of Fe-18Mn-10Al-0.9C-5Ni steel revealed decreased with increasing aging temperature as shown in the Figure 10 (a). This study also involved the Vickers microhardness for the age hardenability of constituent phases such as ferrite/B2 stringers and γ-austenite in the aging condition at 500 °C and for up to 10 hours as shown in Figure 10 (b). Both phases got increases in hardness, but better age hardenability was remarked on ferrite/B2 stringers. So, it is noted that the hardness of low-density steel is closely connected to the distribution and the growth of κ-carbide precipitates during precipitation hardening.

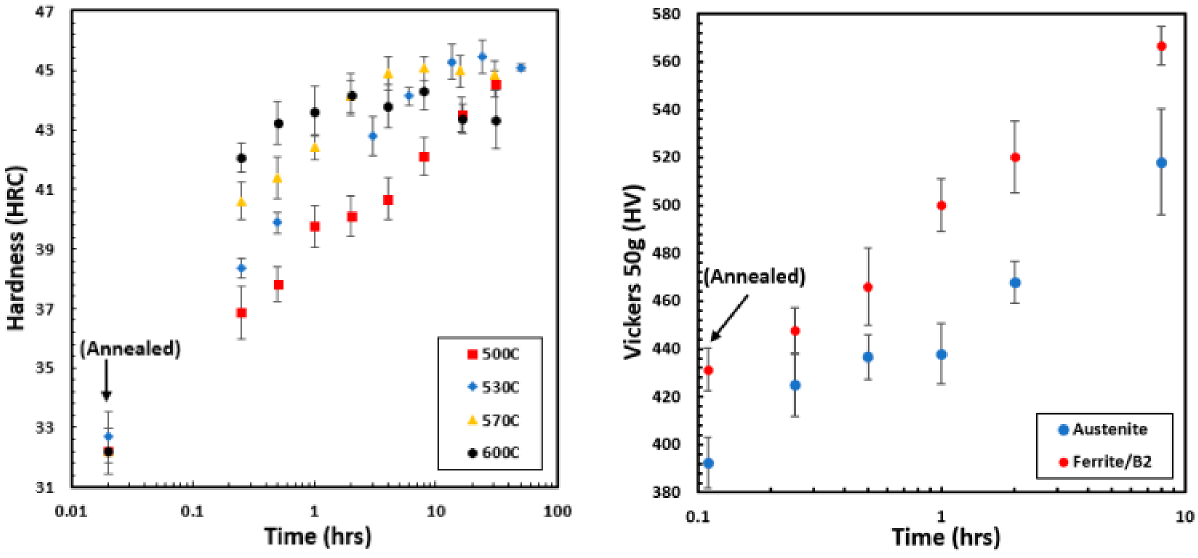

(a) (b)

Figure 10: Hardness Rockwell C (a) and Vickers hardness (b) measurement on Fe-18Mn-10Al-0.9C-5Ni with different ageing times and temperature (500, 530, 570, and 600 °C) [51]

Wu et al. [51] measured strength, strain hardening rate, and total elongation from the tensile tests on Fe-26Mn-8/10Al-1C alloys, which were prepared by solution treatment, aging for 0.5 hour or aging for 4 hours respectively. All samples have κ-carbides within γ-austenite grains because as-solution treated Fe-Mn-Al-C steel appears to include κ-carbides [27, 51]. The experimental result in Figure 11 showed ultimate tensile strength was the higher for 40 hours aged sample than for 0.5 hours aged sample mainly due to the increased number of nano-sized κ-carbides. But sample aged for longer yielded lower total elongation, and the elongation reduction at failure was more apparent in 10Al than in 8Al. The ductility of materials is closely related to their strain hardening rate. The strain hardening rate of the aged steels decreases with increasing aging time. The work attributed decrease in strain hardening to the change in the density of slip bands with increasing aging time [51, 52].

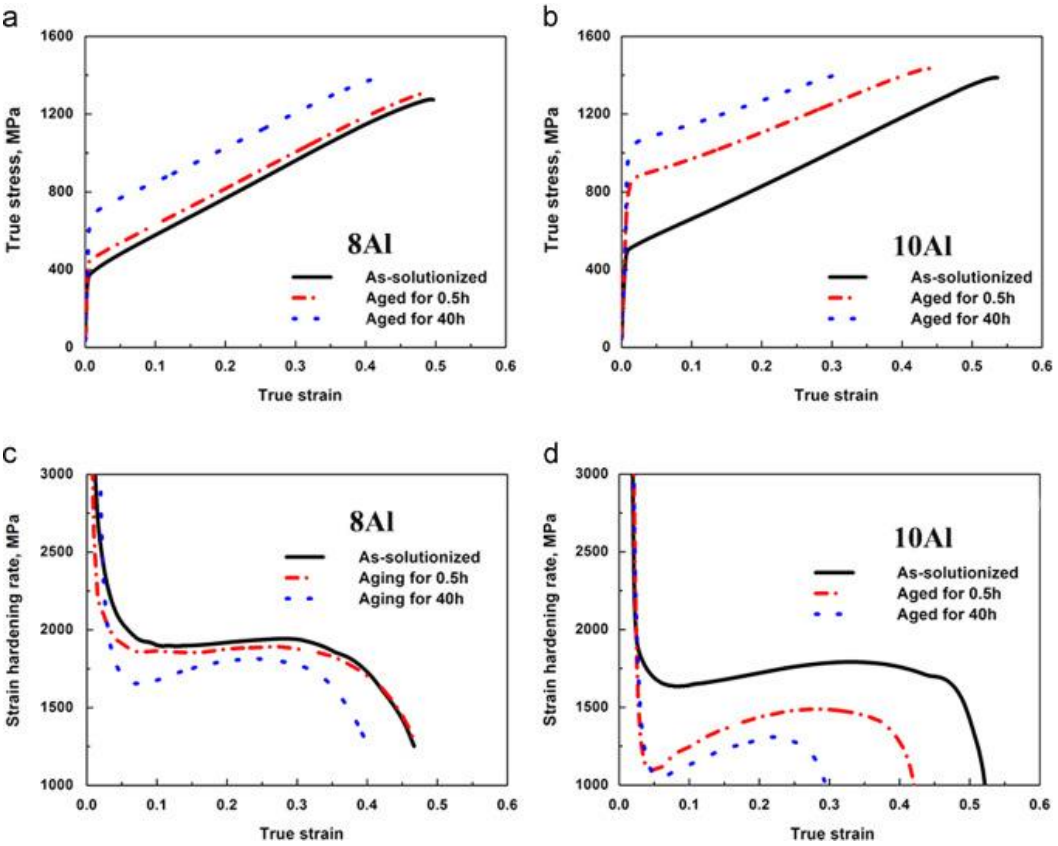

Figure 11: Mechanical properties of Fe-26Mn-8/10Al-1C alloys measured at solution treatment, 0.5-hour ageing, and 4-hours ageing respectively [51]

There are other factors demonstrated by many works to cause elongation reduction besides the change in the density of slip bands. Mondal et al [53]. conducted tensile tests on Fe-37Mn-9.6Al-0.76C (B23) before and after ageing at 550 °C for 8 hours. Tensile test results showed that aged B23 has deteriorated strength and strain. In order to identify the cause of the brittle behavior of B23 after aging, X-ray diffraction analysis (XRD) have been performed on B23 in the as received one and in aged condition. As it can be observed in XRD graphs, as received B23 consists of austenite and a little quantity of ferrite. After aging, intermetallic phases, such as Al8Mn5, FeMn4 and FeMn3, are formed. Hence, this explains that the brittle fracture of aged B23 in the elastic region is derived from the formation of intermetallic phases, which are very brittle that acts as stress intensifiers.

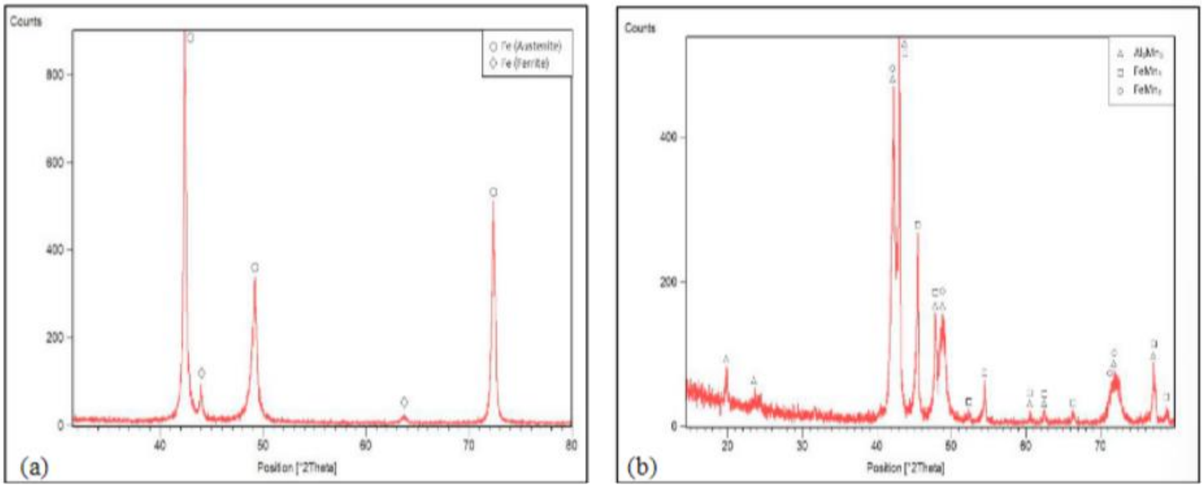

Figure 12: XRD patterns of Fe-37Mn-9.6Al-0.76C (B23) before (a) and after (b) ageing at 550 °C for 8 hours [53]

1.4. THE INFLUENCE OF STRAIN RATE ON MECHANICAL PROPERTIES

Due to the purpose of using low-density steel as structural material in automotive industry, Fe-Mn-Al-C steel has been subjected to measuring influence of strain rate-dependent mechanical properties. To understand the influence of strain rate on plastic behavior, Fe-30Mn-9Al-0.65 alloy was subjected to impact bending test by A. Śmiglewicz and M.B. Jabłońska [54]. After the impact bending test on the initial surface area of 0.8 cm^2 (S) at 7.5, 15 and 30 m/s respectively, the stresses required until fractures (L_U) were computed based on the area under bending force-time graphs at each strain rate as shown in Figure 13. The impact resistance of the alloy at each strain rate was obtained from the calculation using the Eq. 1.

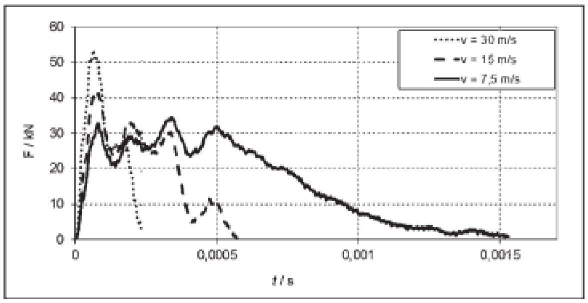

Figure 13. Bending force-time graphs from the impact bending tests on Fe-30Mn-9Al-0.65 alloy at strain rate of 7.5, 15 and 30 m/s respectively [54]

$$U = \frac{L_U}{S}\ [\frac{J}{cm^2}]$$ – Eq. 1 [54]

The experimental results were organized in the table 1. The highest bending force and the highest L_U were achieved at 30 m/s strain rate. It shows faster strain rate led to higher resistance to impact. Therefore, this impact bending tests on Fe-30Mn-9Al-0.65 alloy provides the evidence that strain rate is related to the mechanical properties of low-density steel.

Table 1: Experimental results for impact bending tests on Fe-30Mn-9Al-0.65 alloy at strain rate of 7.5, 15 and 30 m/s respectively [54]

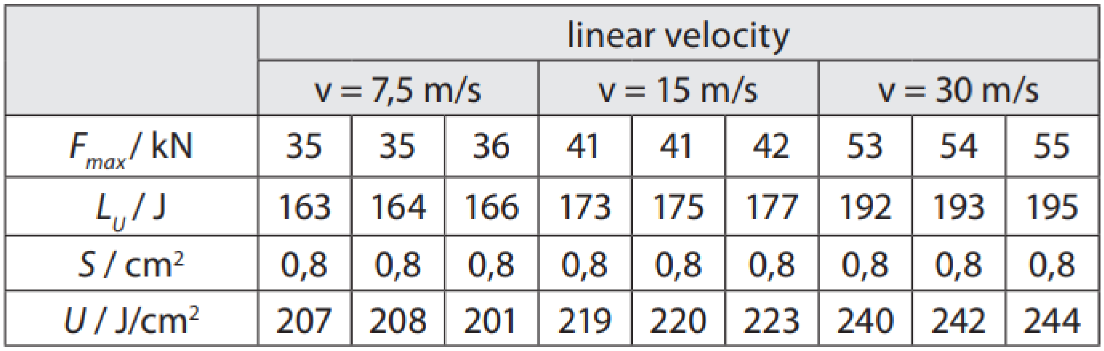

	linear velocity								
	v = 7,5 m/s			v = 15 m/s			v = 30 m/s		
F_{max} / kN	35	35	36	41	41	42	53	54	55
L_U / J	163	164	166	173	175	177	192	193	195
S / cm^2	0,8	0,8	0,8	0,8	0,8	0,8	0,8	0,8	0,8
U / J/cm^2	207	208	201	219	220	223	240	242	244

Lee et al. [55] conducted tensile test on Fe-12Mn-0.6C-0.06N steel at strain rates from $10^{-1}s^{-1}$ to $10^{-5}s^{-1}$ and observed the influence of strain rate on changed dominant deformation mechanism. When it comes to mechanical properties, the increase of UTS by 200 MPa and better e_t that reaches ≈500 % were demonstrated at strain rate of $10^{-1}s^{-1}$ in comparison of e_t of ≈150 % obtained at $10^{-5}s^{-1}$ strain rate. As a root cause of such improvement, the study pointed that dominant strain hardening differs from strain rates; At the strain rates slower than $10^{-4}s^{-1}$, shear stress for TRIP activation is lower than one for twinning. So, TRIP dominantly work as deformation method. By contrary, TWIP is activated with lower shear stress than the one for dislocation slip at strain rate higher than $10^{-2}s^{-1}$, thus causing the change of dominant mechanism from TRIP to TWIP throughout $10^{-3}s^{-1}$.

A similar strain rate-dependence on mechanical properties was reported from the study [56] with Fe-25Mn-3Al-3Si alloy in the strain rate range from $10^{-4}s^{-1}$ to $10^{2}s^{-1}$. Figure 14 has similar UTS and e_t behaviors with increasing strain rates as with the Lee et al [55]. It was also noted that greater sample thickness enhances UTS and e_t. But the change of dominant deformation mechanism was not observed with increasing strain rate as mechanical twins and ε-martensite laths were present at all the strain rates under dark-field transmission electron microscopy.

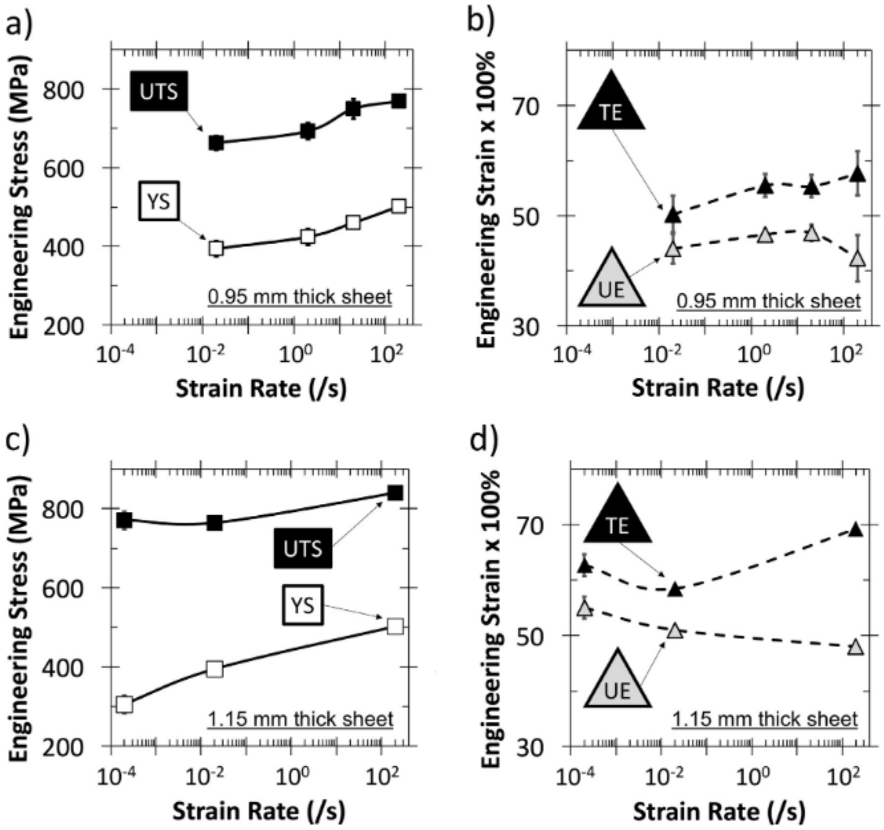

Figure 14: Mechanical properties of Fe-25Mn-3Al-3Si measured in the strain rate range from $10^{-4}s^{-1}$ to $10^{2}s^{-1}$ [56]

To clarify the influence of strain rate on strain hardening mechanism, Kalidindi tracked the behavior of mechanical twins at different strain rates under SEM observation [57]. In Figure 15 (a), $10^{-3}s^{-1}$ had the lowest true stress and no twin formation on Fe-18Mn-1.6Al-0.57C alloy. In Figure 15 (b), after stage A, where strain hardening temporarily deteriorated due to dislocation storage reduced from cross slip and dislocation annihilation, strain hardening rates at the other strain rates rebounded with mechanical twin formation [57-61]. However, strain hardening rate at $10^{-3}s^{-1}$ kept reduced with no twin formation. From the slope of strain hardening rates, it was also able to notice that greater volume fraction of twinning was attained from faster strain rate. Based on literature review, our study will identify the influence of ageing and strain rate on the mechanical properties of Fe-0.92C-26.3Mn-8.79Al-0.05Nb so that will contribute to optimization of post-thermal treatment of hot rolled Fe-0.92C-26.3Mn-8.79Al-0.05Nb alloy.

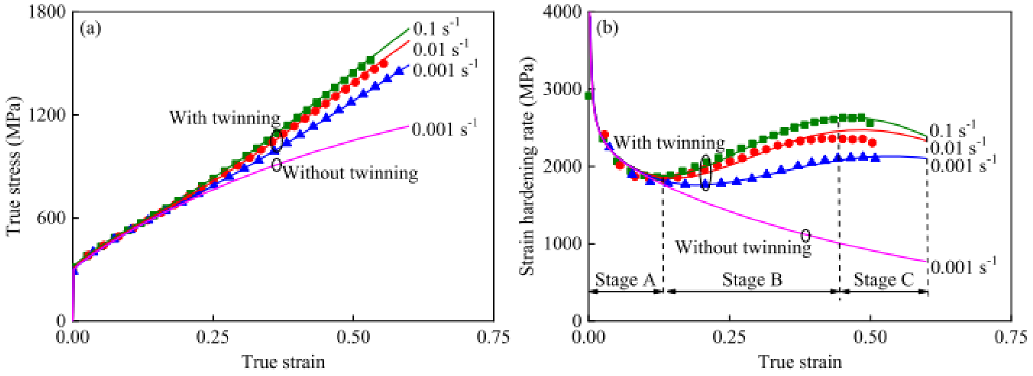

Figure 15: Twinning behavior as a function of strain rate on Fe-18Mn-1.6Al-0.57C alloy [57]

CHAPTER 2: MATERIALS AND EXPERIMENTAL METHODS

2. EXPERIMENT

Experimental Fe-Mn-Al-C-Nb steel with nominal chemical composition of Fe-0.92C-26.3Mn-8.79Al-0.05Nb was melted in a 15 kg vacuum induction melting furnace. The as-cast ingot of 10 in (l) x 5 in (w) x 5 in (t) was thermo-mechanically rolled via multiple passes. The samples were annealed at 900 °C for 4 h and quenched in water, followed by aging at 550 °C for 20 h to form high density κ-carbides in the steel. The accepted theories about κ-carbides formation were explained in aforementioned references [1-4]. Nb was added in the experimental steel to enhance the strength of steel through solid-solution and/or precipitation strengthening effects. Uniaxial tensile experiments were performed at a strain rate of 5.2×10–4·s–1 using tensile testing equipment. Strain was measured using an electronic extensometer. The experimental steel was sawed into five pieces with 5mm thickness at feeding speeds of 5-10 mm/s in Buehler IsoMet 1000. The cut pieces were placed at 550 °C inside the Thermolyne benchtop muffle furnace for different ageing times (1, 10, 25, 50, and 75 hours). After the age heat treatment at 550 °C for different times, Bruker D8 Focus X-ray diffraction scanned the aged steel pieces in the range of 2θ=20–100º to find microstructural change during ageing. Vickers hardness at room temperature was measured with 1.0 kgf indentation load using Wilson VH1202 Micro Hardness Tester. The hardness-ageing time graph from the Vickers hardness test will explain how age hardening contributes to the mechanical properties of the experimental steel. As sample preparation to microstructural observation, hot compression mounted samples using the Buehler SimpliMet 3000 and the PhenoCure were polished with Buehler AutoMet 250 and then etched with Kroll's reagent. The prepared 1 h and 75 h aged samples were observed under the Olympus GX53 optical microscope and Hitachi SU3500 scanning electron microscope in order to comprehend microstructural evolution as a function of ageing time. The different grain size and the width of annealing twins were determined on obtained optical and SEM images in the aid of Image J software. Lastly, the effect of strain rate on hardness values was studied at room temperature with Keysight Nano Indenter G200. The experimental set-up of which consisted of a Berkovich three-sided pyramidal diamond indenter with an angle of 65.3° and an indenter tip of 20 nm diameter; During indentation, mounted samples were indented with 1000nm depth limit and at different strain rates of 0.1, 0.5, and 1.0 s^{-1}. Resulting hardness-displacement graph for all the strain rates will be presented in result and discussion section. The study enabled the optimization of post-thermal treatment on Fe-Mn-Al-C-Nb low-density steel.

CHAPTER 3: RESULTS AND DISCUSSION

3.1. RESULTS AND DISCUSSION

To support a qualitative assessment of the phase transformation sequence during ageing, X-ray diffraction analyses were carried out with 10 h and 50 h aged sample at 550°C. Compared to XRD peaks of fully austenitic Fe-37.55-8.5Al-0.6C steel from Khani et al [62]., XRD patterns in the range of 2θ = 20-100 in Figure 16 demonstrate the dominant austenitic phase in the microstructure. No other phases such as M3C, β-Mn, $D0_3$ and B2 were identified in the 10 h aged sample, whereas the peak relevant to $D0_3$ or B2 appeared in XRD pattern of 50 h aged sample as aged Fe-30Mn-10.5Al-1.1C-3Mo steels in Moon et al [63].

X-ray diffraction patterns of 2θ = 20-100 were drawn in Figure 16 for the two experimental steels aged at 550°C for 10 h and 50 h each. In comparison to the XRD of fully austenitic Fe-37.55-8.5Al-0.6C steel from Khani et al [62]., The existence of austenite as a dominant phase in 10 h and 50 h aged samples was proved in this figure. As noticed, 50 h aged sample exhibit lessen intensities at certain peaks and sideband reflection peaks in its XRD pattern. (200)γ peak dramatically changed over the course of 50 h ageing, having sideband reflection, in which the (200)κ’ reflection peak due to C-rich κ’ carbides appears on the low-angle side of (200)γ peak [64]. 50 h sample has broadening peaks as well, and the broadening of peaks is generally analyzed with the Scherrer equation along which the full width at half maximum is inversely proportional to the grain size. However, as explained regarding to Figure 17 and 18, the grain size of experimental steels turns out to be larger with longer ageing time. So, there needs to be another concept to broadening phenomena of peaks. The study by Balogh et al. [65], correlating twins with XRD pattern in face-centered cubic structure, identified that symmetric broadening of XRD peaks is made by twin boundary formation. On the other hand, the increase in intrinsic and extrinsic stacking faults led to asymmetric broadening. As measured in Figure 19 and 20, ageing contributes to the formation and growth of annealing twins in experimental steels. So, sub reflection of X-ray by twin boundaries can be utilized for broadening peaks.

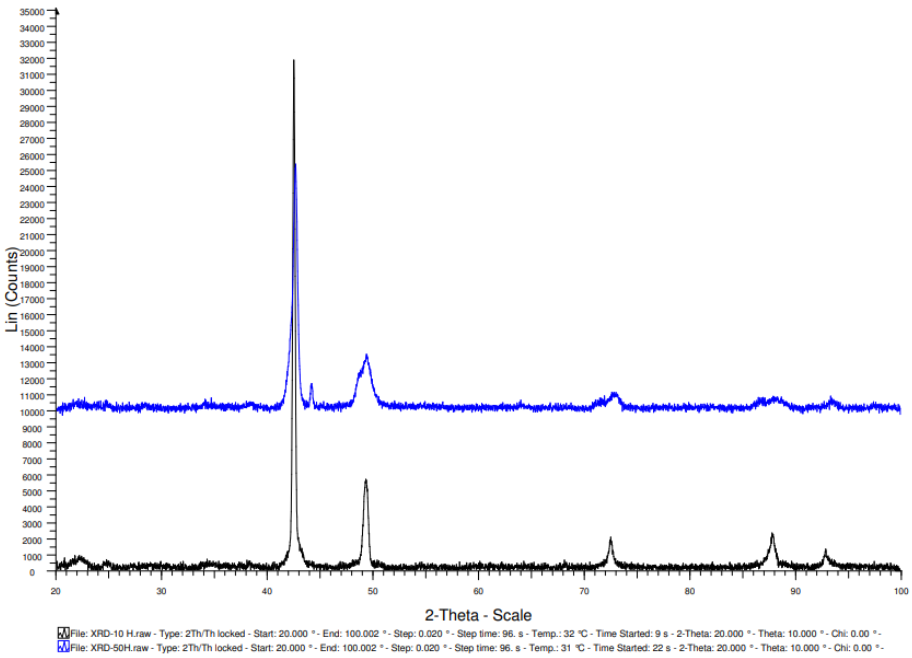

Figure 16: XRD patterns for 10 h and 50 h aged Fe-0.92C-26.3Mn-8.79Al-0.05Nb alloys at 550°C

Optical micrographs of Fe-0.92C-36.3Mn-8.79Al-0.05Nb steels, aged at 550°C for 1 and 75 h respectively, are shown in Figure 17 and 18. As noticed from those figures, the austenitic grain size increases with longer ageing time. The average grain size of both 1 and 75 h aged samples was calculated by making average values after dividing lines of known lengths by each number of intersecting grain boundaries in aid of Image J software. So, their average grain sizes were determined to be 10.56 and 15.82 μm for 1 h and 75 h aged samples, respectively. When the optical micrograph is analyzed, there exist intergranular and intragranular κ-carbides. For 1 h ageing, intragranular κ-carbides are small and evenly dispersed whereas intergranular κ-carbides along grain boundaries are easily found due to larger sizes. For 75 h ageing, intragranular κ-carbides features grown size and globular shape, and δ-ferrite stringer is observed to be existent based on brighter contrast and band-like shape as compared to Huo et al. [65].

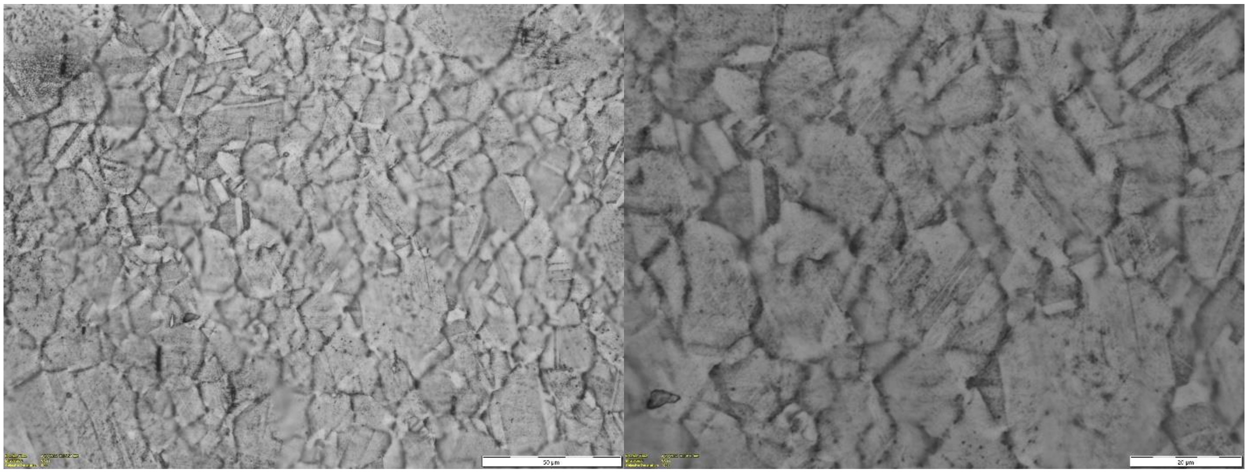

Figure 17: Optical micrograph 500X (left) and optical micrograph 1000X (right) obtained on 1 h-550°C aged sample

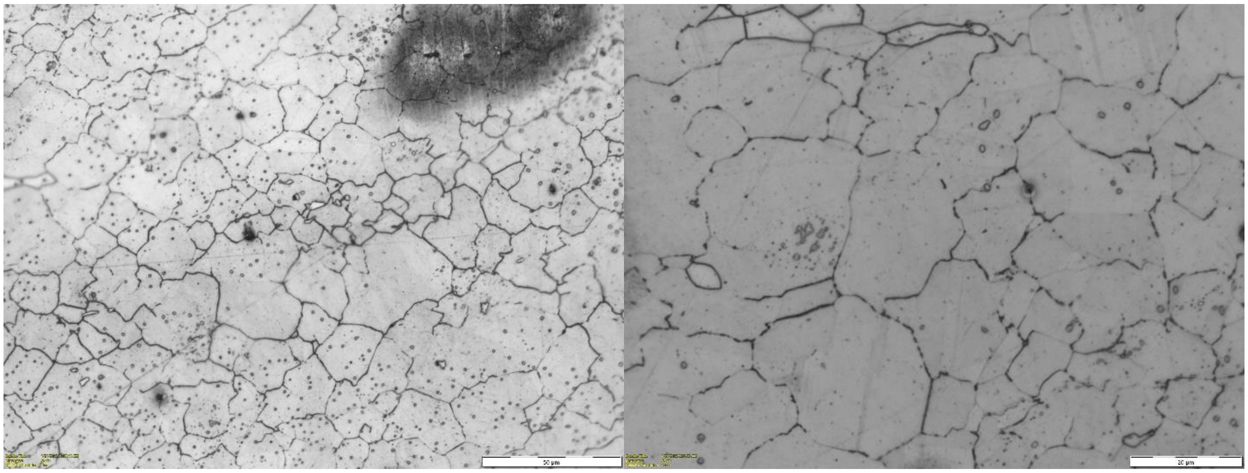

Figure 18: Optical micrograph 500X (left) and optical micrograph 1000X (right) obtained on 75 h-550°C aged sample

According to SEM, the SEM images of 1 h and 75 h aged samples show equiaxed grains and twins inside of grains. The growth of twins as function of ageing time was observed in Figure 19 and 20. The width measurement of twins on SEM images of each sample in aid of Image J software clarify that the growth of annealing twins by ageing heat treatment. In the case of 75 h aged sample, intergranular κ-carbides prominently displayed on its image.

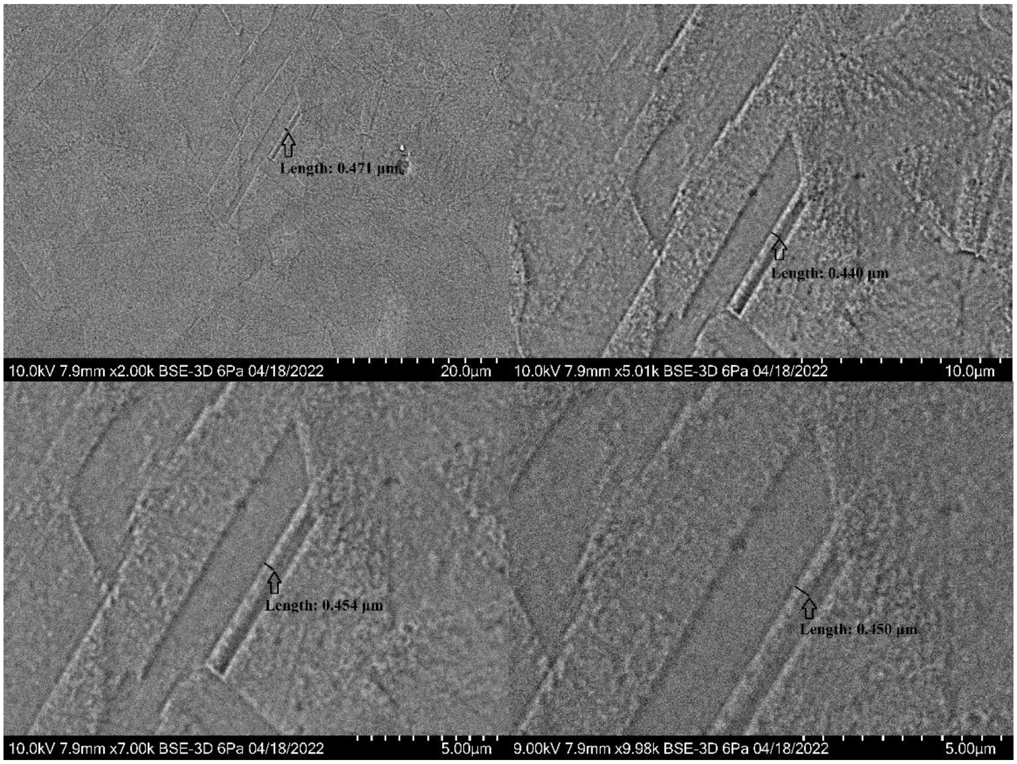

Figure 19: The SEM images (2.00 K, 5.01K, 7.00K, and 10.00K magnifications) pertaining to annealing twin growth on 1 h-550°C aged sample

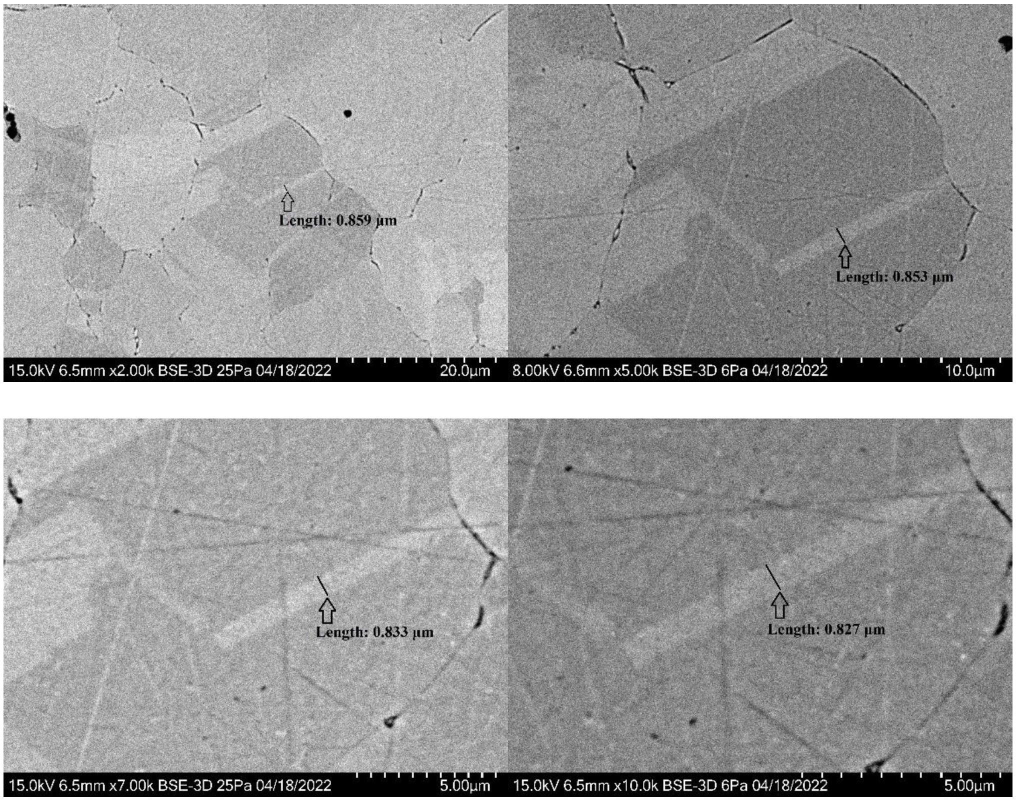

Figure 20: The SEM images (2.00 K, 5.00K, 7.00K, and 10.00K magnifications) pertaining to annealing twin growth on 75 h-550°C aged sample

Figure 21 shows the Vickers hardness as ageing progressed at 550^{o}C. The Vickers hardness increased gradually due to an increase in the fraction of the κ-carbides. Decrease in Vickers hardness was not observed during ageing experimental steel up to 75 h, but Fe-30Mn-10.5Al-1.1C-3Mo in Moon et al. [63] reached their peak hardness at around 80000 s of ageing at 675^{o}C and showed gradual decrease due to over-ageing cause by the saturation of beta-Mn and the softening effect during aging.

Table 2: Tensile properties for as-roll, STQ@1h-950^{o}C, 20 h-550^{o}C aged alloys

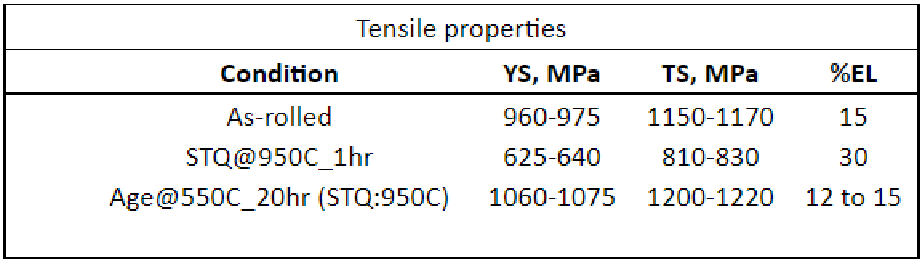

Tensile properties

Condition	YS, MPa	TS, MPa	%EL
As-rolled	960-975	1150-1170	15
STQ@950C_1hr	625-640	810-830	30
Age@550C_20hr (STQ:950C)	1060-1075	1200-1220	12 to 15

The deformation mechanism of experimental steel can be assumed from stacking fault energy. Considering the conventional knowledge that dominant deformation mechanism becomes the deformation twinning in the SFE range between 22 and 45 mJ m^{-2}., the expected mechanism of experimental steel based on the studies with similar chemical compositions should display dislocation gliding. However, both mechanical twinning and dislocation gliding were observed in the relevant studies. So, it is confirmed that the experimental steel has ability to make mechanical twinning and dislocation glide during strain. During tensile test on experimental steels, mechanical twining is possible to occur. The primary model for mechanical twining is proposed by Mahajan and chin [66]. According to the mechanism, two perfect dislocations split into fault pairs and react on the primary slip plane to produce three Shockley partial dislocations on adjacent planes. The Shockley partial dislocations in each stacking fault are separated by the balance of attractive forces due to the stacking fault and the repulsive forces due to the partial dislocation. the force necessary to bring about partial dislocation in stacking faults requires stress concentration to be achieved by a dislocation pile-up. because of repulsive force between the two partial dislocations, atoms in the core of partial dislocation can rearrange so that it can glide on the adjacent slip plane. If a third fault pair approaches on side of this double stacking fault arrangement, the original two partials can combine and move to the next adjacent layer and slip away, creating a three-layer stacking fault. The Shockley partials on one side of the stacking fault form an interface whose Burgers vectors sum to zero, making the interface immobile under the applied stress. This leaves the Shockley partials on the opposite side of the stacking fault that is free to move away from the interface. Therefore, the mechanical twinning is formed by the reaction of perfect dislocations with different slip systems in the same plane. Three-layer stacking fault was found as twin nucleation mechanism in FCC materials by Mahajan and chin [66, 68], and Bracke et al [67, 68]. and mechanical twining by three-layer stacking fault model was confirmed to be main strain hardening mechanism in TWIP steel by Steinmetz et al [68]. Therefore, mechanical strengths of all the samples basically originate from mechanical twining during tensile tests.

The deformation twins act as planar obstacle as pinning center for gliding dislocation so that reduce the mean free path of dislocation glide. Dislocations pile up at interfaces between twins and austenite matrix phase and cause significant back stress that impede the progress of accumulated dislocations. These back stresses contribute a significant amount to the required flow stress, thus increasing the work-hardening rate.

In Table 2, compared to solution treated sample at 950^{o}C for 1 h, mechanical properties of as-rolled sample showed both yield strength and ultimate tensile strength increased by 30%. The dislocations formed by cold-rolling piles up at either grain boundaries or twin boundaries. This dislocation pile-up makes dislocation movements difficult, thus leading to the higher values in mechanical properties. Cold rolling high Mn steel containing deformation twins and slip bands by Park et al. [69] demonstrated that the cold working induces deformation twinning in the austenite grains, and the density of twinning increased with larger reduction. Which result in Hall-Petch relationship considering the twins boundaries [70]. Therefore, effective blocking to dislocation motion induced by strain hardening provides strengthening effect to mechanical properties whereas the ductility of experimental steel decreases by half.

For solution treated sample at 950°C for 1 h, yield strength and ultimate tensile strength are decreased but elongation increased double compared to as rolled sample. Similar behavior of mechanical properties was obtained from Ji et al [71]. Despite mechanical twinning still exists as strengthening mechanism during deformation, yield strength went down to 625-640 MPa, and ultimate tensile strength decreased to 810-803 MPa. The decrease in the strengths results from the dislocation annihilation and grain coarsening. Since the number of dislocations decreases from annealing, dislocation pile-up that block dislocation motion lessened so that dislocations are easier to move. Whereas the refined austenite grain size enhances the increase in mechanical properties due to the Hall-Petch relationship, $\sigma = \sigma_0 + k/d^{-0.5}$ [71, 72], annealing recrystallization led to the decrease in mechanical properties. However, higher total elongation was granted from the increase in grain size after annealing [71-73].

As compared to the as rolled, the increase in the yield strength and the ultimate tensile strength was achieved from the aged sample at 550°C for 20 h. κ-carbides precipitation is the main hardening mechanism during ageing because κ-carbides coherent with austenite matrix work as effective obstacles to dislocation movement. The response of Fe-31.4Mn-11.4Al-0.89C steel to ageing at 550°C describes possible hardening factors under ageing [74]. At the early stage up to 20 h, the nano-sized κ-carbides in the austenite matrix effectively gave strengthening. The mechanical properties enhanced by micro/nano κ-carbides has been reported from other previous studies as well [74-79]. After the stage of κ-carbides formation, β-Mn and ordered bcc phases (B2 or D03) were observed to make remarkable contributions to the increased hardness

[74, 79]. However, β-Mn was not detected under experimental ageing times as seen from the XRD graph of 50 h aged sample in Figure 16 and Vickers hardness values in Figure 21.

The linear tendency of Vickers hardness graph in Figure 21 exhibited that κ-carbides are the main factor of age hardening, and the XRD graph of 50 h aged sample implied that age hardening varies along with the alloying composition, showing the presence of B2 and D03 phases except β-Mn. The total elongation of the aged sample was reduced to the half total elongation of solution treated sample at 950°C for 1 h. As observed from Figure 20, the reduced ductility resulted from the existence of coarsened intergranular κ-carbides. The κ-carbides within the austenite grain boundaries made experimental steels brittle because they accelerate crack propagation during deformation.

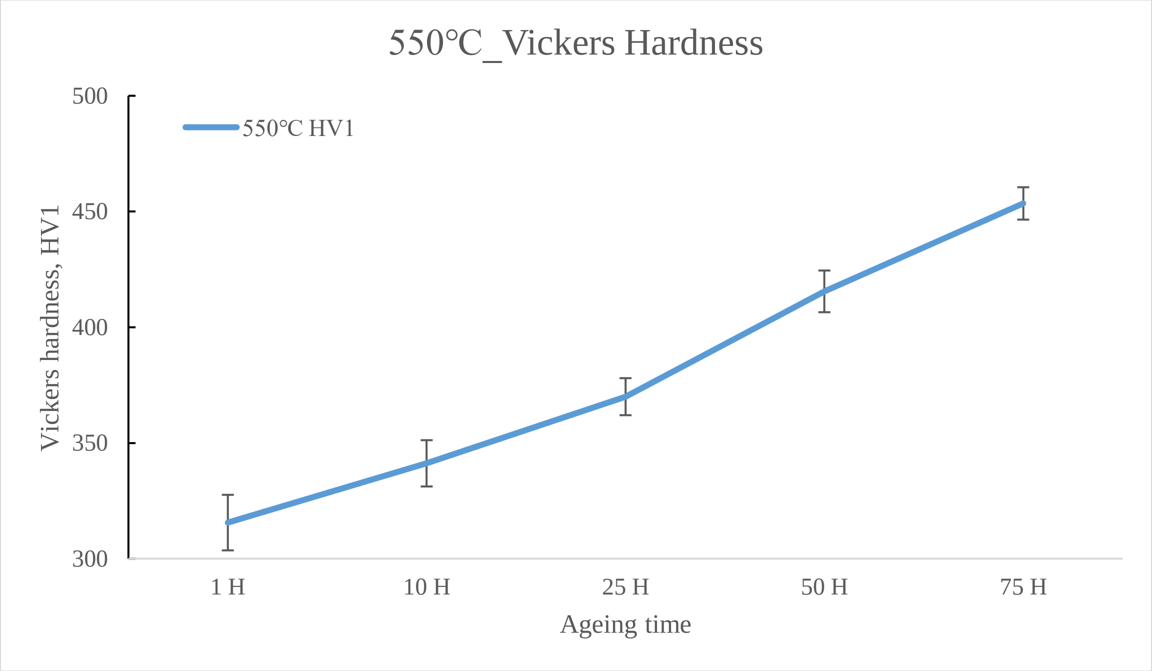

Figure 21: Vickers hardness for 550°C aged alloys as a function of ageing time

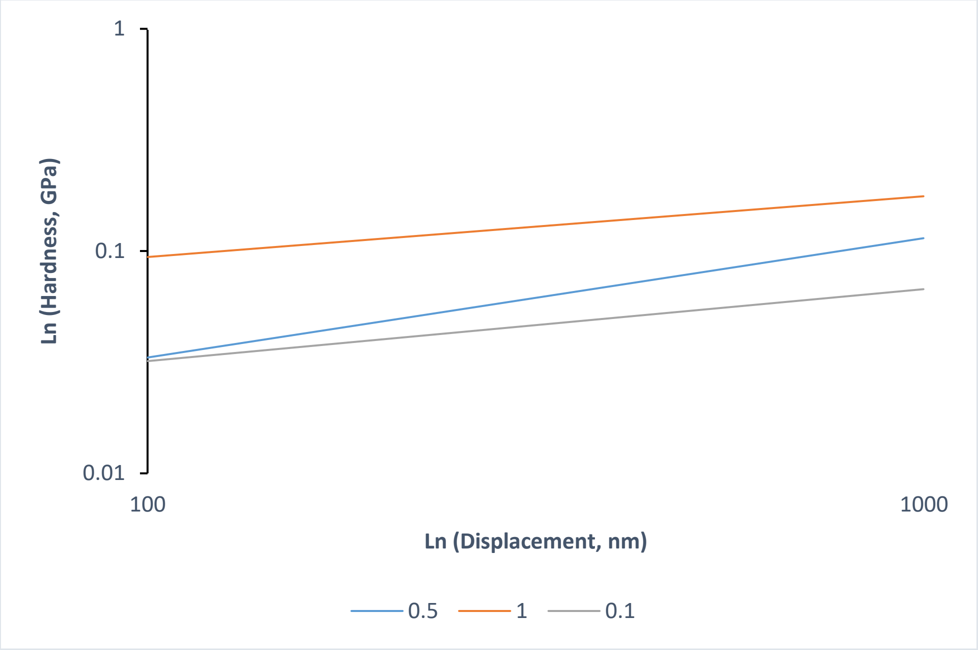

Figure 22: The Ln hardness-Ln displacement graph from nanoindentation test at the strain rates of 0.1, 0.5, and 1 s^{-1}

Lastly, the effect of strain rate was evaluated from nanoindentation test on 25 h-550^{o}C aged sample. At different strain rates of 0.1, 0.5, and 1 s^{-1}, Ln hardness-Ln displacement graph in Figure 22 demonstrates the relationship between hardness values and strain rates; hardness value increases as a function of strain rate because dynamic Hall-Petch relationship considering twin formation [80-84] effectively confines the movement of dense dislocations within intra-twin regions, thus reducing a mean free path of dislocation glides [80, 85-87]. From the compressive test on Fe-30Mn-9Al-1.0Si-0.9C-0.5Mo alloy at a strain rate of 3000 s^{-1}, shear bands exhibited their growth through the rotation of numerous slips towards adjacent shear bands as deformed. Adiabatic shear bands formed by slip plane reorientation and local heat generation strain hardened the alloy until fracture [88]. TEM observation for straining high Mn austenitic steel witnessed that the volume fraction of secondary twins diminished in the steel with coarser grain size. However, the total fraction of mechanical twins turned out to proportionally increases along straining degree, thus leading to work hardening [77]. Another study observed [89] evident deformation transition from dislocation glide to deformation twinning as a function of strain rate. At the lowest strain rate of 0.01 s^{-1}, dislocation glide was the main contributor to deformation mechanism. With faster strain rate, greater shear stress localization due to faster shear strain made stacking faults have wider width. That caused the critical shear stress for dislocation glide to be higher than that for mechanical twin. As a result, the study drove increased hardness values from nano-indentation tests with increasing strain rate up to 1 s^{-1}. Despite of previous studies, the detailed research on the effect of strain rate at different ranges of temperatures was not conducted to the best of author's knowledge. Therefore, this will be dealt in the follow-up study.

3.2. CONCLUSIONS

In the present study, a hot-rolled Fe-0.92C-26.3Mn-8.79Al-0.05Nb alloy was subjected to various tests to study the effect of age time and strain rate on mechanical properties. In order to find microstructural evolution as a function of age time, the alloy was subjected to X-ray diffraction, scanning electron microscopy, and optical microscopy. The samples aged at different times was used for the measurement of Vickers hardness, nano-indentation test was conducted on 25 h-550^{o}C aged sample at the strain rates of 0.1, 0.5, and 1.0 s^{-1} drawing a Ln hardness-Ln displacement graph.

XRD analysis on 10 h-550°C and 50 h-550°C aged alloys revealed austenitic matrix. In scanning range of $2\theta = 20\text{-}100^{o}$, 50 h-550°C aged alloy had lower intensity of $(200)\gamma$ peak and sideband reflection of $(200)\kappa$ peak due to C-rich κ-carbide precipitation as compared to 10 h-550°C aged alloy. As a results of ageing, broadening peaks were observed from 50 h-550°C aged alloy. This symmetrically broadening phenomena was attributed to the twin boundary formation. XRD peak related to $D0_3$ or B2 phase from 50 h-550°C aged sample also denoted the presence of additional phase besides κ-carbide.

Grain sizes were measured on 1 h-550°C and 75-550°C aged samples under optical microscopy. In the aid of Image J software, the average grain sizes were determined to be 10.56 and 15.82 μm for 1 h and 75h aged samples respectively. This verifies that Scherrer equation is not applicable to explain the broadening XRD peaks observed from 50 h-550°C aged sample.

The growth of annealing twins was identified from SEM images of 1 h and 75 h aged samples. To measure the width of annealing twins with Image J software gave the average values of 0.454 μm and 0.843 μm for 1 and 75 h aged sample respectively. Intergranular precipitation of κ-carbide was also observed on the SEM images of 75 h aged sample.

550^{o}C-20 h aged sample was subjected to tensile test to compare tensile properties of age hardened sample with samples that had been through other post-treatment. The result showed the highest yield strength and ultimate tensile strength in 550^{o}C-20 h aged sample, but 12-15% ductility, the half ductility of the STQ 950-1h sample. As observed in 75 h aged sample, the ductility reduction resulted from the presence of coarsened intergranular κ-carbides that are the source of cracking. The coherency strengthening of κ-carbides within austenitic matrix and coarsening of κ-carbides were appointed as main strain hardening mechanisms. It can be shown in Figure 21 that Vickers hardness values are associated with the precipitation and coarsening of κ-carbides during age heat treatment. Reduced hardness value owing to over-ageing was not observed under the range of ageing times. Since ordered bcc phases (B2 or D03) are known to contribute to the increase in hardness [74, 79], XRD peak related to B2 and D03 phases from 50 h aged sample implies their contribution to high tensile properties of samples aged for 50 h and longer.

For 25 h -550^{o}C aged sample, nano-indentation hardness tests were conducted at the strain rates of 0.1, 0.5, and 1 s^{-1} to investigate the relationship between hardness and strain rate. resulting Ln hardness-Ln displacement graph shows that the hardness value gets higher with increasing strain rate because of dynamic Hall-Petch relationship; in which the formation of primary and secondary mechanical twins is proportional to strain rate. stress localization at faster strain rate makes the critical stress for dislocation glides higher than that for mechanical twins. As a result, the formation of mechanical twins is activated prior to dislocation movements.

REFERENCES

1. Bentley, A. P. “Ordering in Fe-Mn-Al-C Austenite - Journal of Materials Science Letters.” SpringerLink, Kluwer Academic Publishers, 1986.
2. Zhang, Jianlei, et al. “Revisiting the Formation Mechanism of Intragranular κ-Carbide in Austenite of a Fe-Mn-Al-Cr-C Low-Density Steel.” Scripta Materialia, Pergamon, 10 Mar. 2021.
3. Moon, Joonoh, et al. “Atomistic Investigations of κ-Carbide Precipitation in Austenitic Fe-Mn-Al-C Lightweight Steels and the Effect of Mo Addition.” Scripta Materialia, Pergamon, 14 Sept. 2016.
4. Mapelli, C., et al. “Γ Decomposition in Fe–Mn–Al–C Lightweight Steels.” Journal of Materials Research and Technology, Elsevier, 3 Mar. 2020.
5. Kim, Sung-Dae, et al. “Strain Hardening Recovery Mediated by Coherent Precipitates in Lightweight Steel.” Nature News, Nature Publishing Group, 14 July 2021.
6. Mishra, Sumeet, et al. “A New Phenomenological Approach for Modeling Strain Hardening Behavior of Face Centered Cubic Materials.” NASA/ADS, 2019.
7. Sato, Kazunori, et al. “Spinodal Decomposition and Mechanical Properties of an Austenitic Fe-30wt.%Mn-9wt.%Al-0.9wt.%c Alloy.” Materials Science and Engineering: A, Elsevier, 17 Apr. 2003.
8. Sato, Kazunori, et al. “Modulated Structure and Magnetic Properties of Age-Hardenable Fe-Mn-Al-C Alloys - Metallurgical and Materials Transactions a.” SpringerLink, Springer-Verlag, 1990.

9. Bartlett, Laura N., et al. “An Atom Probe Study of Kappa Carbide Precipitation and the Effect of Silicon Addition - Metallurgical and Materials Transactions a.” SpringerLink, Springer US, 20 Feb. 2014.
10. Cheng, Wei-Chun, et al. “Phase Transformation of the L12 Phase to Kappa-Carbide after Spinodal Decomposition and Ordering in an Fe–C–Mn–Al Austenitic Steel.” Materials Science and Engineering: A, Elsevier, 2 July 2015.
11. Seol, Jae-Bok, et al. “Direct Evidence for the Formation of Ordered Carbides in a Ferrite-Based Low-Density Fe–Mn–Al–C Alloy Studied by Transmission Electron Microscopy and Atom Probe Tomography.” Scripta Materialia, Pergamon, 17 Aug. 2012.
12. Lu, W J, et al. “Structure and Properties of κ-Carbides in Duplex Lightweight Steels.” Taylor and Francis Online, Ironmaking & Steelmaking , Apr. 2015.
13. Mapelli, Carlo, et al. “JMAK Model Applied on the κ-Carbide Precipitation in FEMNALC Steels.” Journal of Materials Research and Technology, Elsevier, 4 Oct. 2021.
14. Lu, W.J., et al. “K-Carbide Hardening in a Low-Density High-Al High-MN Multiphase Steel.” Materials Letters, North-Holland, 2 Oct. 2014.
15. Kim, Chiwon, et al. “Influence of Inter/Intra-Granular κ-Carbides on the Deformation Mechanism in Lightweight FE-20MN-11.5al-1.2C Steel.” Materials Characterization, Elsevier, 17 Jan. 2020.
16. Sato, Kazunori, et al. “Effects of Deformation Induced Phase Transformation and Twinning on the Mechanical Properties of Austenitic Fe–Mn–Al Alloys.” ISIJ International, The Iron and Steel Institute of Japan, 31 May 2007.

17. Pierce, D.T., et al. “The Influence of Stacking Fault Energy on the Microstructural and Strain-Hardening Evolution of Fe–Mn–Al–Si Steels during Tensile Deformation.” Acta Materialia, Pergamon, 31 Aug. 2015.
18. Grässel, O, et al. “High Strength Fe–Mn–(Al, Si) Trip/TWIP Steels Development - Properties - Application.” International Journal of Plasticity, Pergamon, 28 Aug. 2000.
19. Frommeyer, G., et al. “Physical and Mechanical Properties of Iron-Aluminium-(Mn, Si) Lightweight Steels: Metallurgical Research & Technology.” Cambridge Core, EDP Sciences, 25 Oct. 2002.
20. Haupt, Marco, et al. “The Influence of Warm Rolling on Microstructure and Deformation Behavior of High Manganese Steels.” MDPI, Multidisciplinary Digital Publishing Institute, 18 July 2019.
21. Kuhlmann-Wilsdorf, D. “Theory of Plastic Deformation: - Properties of Low Energy Dislocation Structures.” Materials Science and Engineering: A, Elsevier, 21 May 2003.
22. Kim, Sung-Dae, et al. “Direct Observation of Dislocation Plasticity in High-MN Lightweight Steel by in-Situ Tem.” Nature News, Nature Publishing Group, 23 Oct. 2019.
23. Kang, Li, et al. “Enhanced Mechanical Properties of Fe-Mn-Al-C Low Density Steel via Aging Treatment.” Frontiers, Frontiers, 1 Jan. 1AD.
24. Khatami-Hamedani, H., et al. “Dynamic Restoration of the Ferrite and Austenite Phases during Hot Compressive Deformation of a Lean Duplex Stainless Steel.” Materials Science and Engineering: A, Elsevier, 5 May 2020.
25. Yang, Fuqiang, et al. “Tensile Deformation of Low Density Duplex Fe–Mn–Al–C Steel.” Materials & Design, Elsevier, 23 Mar. 2015.

26. Yoo, Je Doo, and Kyung-Tae Park. “Microband-Induced Plasticity in a High MN–Al–C Light Steel.” Materials Science and Engineering: A, Elsevier, 31 May 2008.
27. Park, Kyung-Tae, et al. “Stacking Fault Energy and Plastic Deformation of Fully Austenitic High Manganese Steels: Effect of Al Addition.” Materials Science and Engineering: A, Elsevier, 26 Feb. 2010.
28. Ma, Tao, et al. “Microband-Induced Plasticity in a NB Content Fe–28Mn–10al–C Low Density Steel.” MDPI, Multidisciplinary Digital Publishing Institute, 19 Feb. 2021.
29. Pierce, D T, and J A Jiménez. “The Influence of Manganese Content on the Stacking-Fault and Austenite ...” Sciencedirect, Acta Materialia , Apr. 2014.
30. Medvedeva, N.I., et al. “First-Principles Study of Mn, Al and C Distribution and Their Effect on Stacking Fault Energies in FCC Fe.” Journal of Alloys and Compounds, Elsevier, 23 Aug. 2013.
31. Chen, Shangping, et al. “Current State of Fe-Mn-Al-C Low Density Steels.” Progress in Materials Science, Pergamon, 31 May 2017.
32. Chen, Peng, et al. “The κ-Carbides in Low-Density Fe-Mn-Al-C Steels: A Review on Their Structure, Precipitation and Deformation Mechanism.” MDPI, Multidisciplinary Digital Publishing Institute, 29 July 2020.
33. Pang, Jingyu, et al. “Tensile Behavior and Deformation Mechanism of Fe-Mn-Al-C Low Density Steel with High Strength and High Plasticity.” MDPI, Multidisciplinary Digital Publishing Institute, 16 Aug. 2019.
34. Castañeda, Jaime A., et al. “Stacking Fault Energy Determination in Fe-Mn-Al-C Austenitic Steels by X-Ray Diffraction.” MDPI, Multidisciplinary Digital Publishing Institute, 26 Oct. 2021.

35. Choi, Young Won, et al. “Predicting the Stacking Fault Energy of Austenitic Fe-Mn-Al (Si) Alloys.” Materials & Design, Elsevier, 29 Nov. 2019.

36. Dumay, A., et al. “Influence of Addition Elements on the Stacking-Fault Energy and Mechanical Properties of an Austenitic Fe–Mn–C Steel.” Materials Science and Engineering: A, Elsevier, 10 May 2007.

37. Dai, Q.X., et al. “Design of Martensite Transformation Temperature by Calculation for Austenitic Steels.” Materials Characterization, Elsevier, 30 July 2004.

38. Li, J.C., et al. “Stacking Fault Energy of Iron-Base Shape Memory Alloys.” Materials Letters, North-Holland, 4 Mar. 1999.

39. Kim, Hansoo, et al. “Fe-Al-Mn-C Lightweight Structural Alloys: A Review on the Microstructures and Mechanical Properties.” Science and Technology of Advanced Materials, Taylor & Francis, 12 Mar. 2013.

40. Sutou, Yuji, et al. “High-Strength Fe-2OMn-Al-C-Based Alloys with Low Density.” Tohoku University, Iron and Steel Institute of Japan, 30 July 2015.

41. T, Park K, et al. “Triple Negative Breast Cancer in Korea-Distinct Biology with Different Impact of Prognostic Factors on Survival.” Breast Cancer Research and Treatment, U.S. National Library of Medicine, 2013.

42. Frommeyer, G., et al. “Physical and Mechanical Properties of Iron-Aluminium-(Mn, Si) Lightweight Steels: Semantic Scholar.” Metallurgical Research and Technology, Rev. Met. Paris, 1 Jan. 1970.

43. Field, Daniel M, and Krista R Limmer. “Alloy Partitioning Effect on Strength and Toughness of κ-Carbide Strengthened Steels.” Oak Ridge National Laboratory, 2022.

44. Takeya, G S, and F E Mariani. “Aging of a Fe-Mn-Al Steel Using Plasma Nitrocarburizing.” Materials Performance and Characterization, 2017.

45. Zambrano, O.A., et al. “Hot Deformation of a Fe-Mn-Al-C Steel Susceptible of κ-Carbide Precipitation.” Materials Science and Engineering: A, Elsevier, 20 Feb. 2017.

46. Cheng, Wei-Chun, et al. “Phase Transformation of the L12 Phase to Kappa-Carbide after Spinodal Decomposition and Ordering in an Fe–C–Mn–Al Austenitic Steel.” Materials Science and Engineering: A, Elsevier, 2 July 2015.

47. Lin, Chih Lung, and Chuen Guang Chao. “Relationship between Microstructures and Tensile Properties of an Fe ...” The Japan Institute of Metals, Materials Transactions, 2010.

48. Zhao, Chao, et al. “Effect of Annealing Temperature on the Microstructure and Tensile Properties of Fe–10Mn–10al–0.7C Low-Density Steel.” Materials & Design, Elsevier, 30 Nov. 2015.

49. Acselrad, O., et al. “Phase Transformations in FEMNALC Austenitic Steels with Si Addition - Metallurgical and Materials Transactions a.” SpringerLink, Springer-Verlag, 2002.

50. Piston, Michael, et al. “Microstructural Influence on Mechanical Properties of a Lightweight Ultrahigh Strength Fe-18Mn-10al-0.9C-5ni (Wt%) Steel.” MDPI, Multidisciplinary Digital Publishing Institute, Sept. 2020.

51. Wu, Z.Q., et al. “Influence of Al Content on the Strain-Hardening Behavior of Aged Low Density Fe–Mn–Al–C Steels with High Al Content.” Materials Science and Engineering: A, Elsevier, 9 May 2015.

52. Choi, Kayoung, et al. “Effect of Aging on the Microstructure and Deformation Behavior of Austenite Base Lightweight Fe–28mn–9al–0.8c Steel.” Scripta Materialia, Pergamon, 3 Aug. 2010.

53. Mondal, A., et al. “Effect of Heat Treatment on Mechanical Properties of FEMNALC Alloys.” Procedia Structural Integrity, Elsevier, 20 Nov. 2021.

54. He, Z.F., et al. “The Effect of Strain Rate on Mechanical Properties and Microstructure of a Metastable Femncocr High Entropy Alloy.” Materials Science and Engineering: A, Elsevier, 21 Jan. 2020.

55. Lee, Sangwon, et al. “Effect of the Strain Rate on the Trip–TWIP Transition in Austenitic Fe-12 Pct MN-0.6 Pct C Twip Steel - Metallurgical and Materials Transactions a.” SpringerLink, Springer US, 12 Oct. 2013.

56. Benzing, J.T., et al. “Effects of Strain Rate on Mechanical Properties and Deformation Behavior of an Austenitic Fe-25MN-3al-3SI TWIP-Trip Steel.” Materials Science and Engineering: A, Elsevier, 8 Nov. 2017.

57. Kalidindi, Surya R. “Incorporation of Deformation Twinning in Crystal Plasticity Models.” Journal of the Mechanics and Physics of Solids, Pergamon, 19 June 1998.

58. Staroselsky, A., and L. Anand. “A Constitutive Model for HCP Materials Deforming by Slip and Twinning: Application to Magnesium Alloy AZ31B: Semantic Scholar.” International Journal of Plasticity, Sciencedirect, 1 Jan. 1970.

59. Sun, C., et al. “Modeling of Slip, Twinning and Transformation Induced Plastic Deformation for TWIP Steel Based on Crystal Plasticity: Semantic Scholar.” International Journal of Plasticity, 1 Jan. 1970.

60. Kocks, U. F., and H. Mecking. “Physics and Phenomenology of Strain Hardening: The FCC Case: Semantic Scholar.” Progress in Materials Science, 1 Jan. 1970.

61. Su, Z X, and N Li. “Strain Rate-Dependent Hardening with Dislocation-Twin Interaction of Fe–Mn–Al–C Steel Using Crystal Plasticity.” Taylor & Francis, 2019.

62. Khani, Rezvan, et al. “Dynamic Strain Aging and Twin Formation during Warm Deformation of a Novel Medium-Entropy Lightweight Steel.” Journal of Materials Research and Technology, Elsevier, 29 Jan. 2022.

63. Moon, Joonoh, et al. “Phase Transformation Mechanism and Hardness during Ageing of an Austenitic Fe-30Mn-10.5al-1.1C-3MO Lightweight Steel.” Journal of Alloys and Compounds, Elsevier, 29 June 2019.

64. Witkowska M, et al. “Microstructural Changes in a High-Manganese Austenitic Fe-Mn-Al-C Steel.” Archives of Metallurgy and Materials, 2014.

65. Balogh, Levente, et al. “Stacking Faults and Twin Boundaries in FCC Crystals Determined by x-Ray ...” Journal of Applied Physics, 2006.

66. Mahajan, S., and G.Y. Chin. “Formation of Deformation Twins in F.C.C. Crystals.” Acta Metallurgica, Pergamon, 11 June 2003.

67. Bracke, L., et al. “Direct Observation of the Twinning Mechanism in an Austenitic Fe–Mn–C Steel.” Scripta Materialia, Pergamon, 29 Mar. 2009.

68. Steinmetz, David R., et al. “Revealing the Strain-Hardening Behavior of Twinning-Induced Plasticity Steels: Theory, Simulations, Experiments.” Acta Materialia, Pergamon, 1 Nov. 2012.

69. Park, Minha, et al. “The Effects of Recrystallization on Strength and Impact Toughness of Cold-Worked High-MN Austenitic Steels.” MDPI, Multidisciplinary Digital Publishing Institute, 29 Aug. 2019.

70. Liang, Z.Y., et al. “The Respective Hardening Contributions of Dislocations and Twins to the Flow Stress of a Twinning-Induced Plasticity Steel.” Scripta Materialia, Pergamon, 18 Sept. 2015.

71. Ji, Fengqin, et al. “Recrystallization Behavior in a Low-Density High-Mn High-Al Austenitic Steel Undergone Thin Strip Casting Process.” Materials Science and Engineering: A, Elsevier, 10 July 2018.
72. Dini, G., et al. “Tensile Deformation Behavior of High Manganese Austenitic Steel: The Role of Grain Size.” Materials & Design, Elsevier, 1 Feb. 2010.
73. Yoo, J.D., et al. “Origin of Extended Tensile Ductility of a Fe-28MN-10AL-1C Steel - Metallurgical and Materials Transactions a.” SpringerLink, Springer US, 7 May 2009.
74. Lee, Keunho, et al. “Investigation of the Aging Behavior and Orientation Relationships in Fe–31.4mn–11.4al–0.89c Low-Density Steel.” *Journal of Alloys and Compounds*, Elsevier, 24 June 2017.
75. Frommeyer, Georg, and Udo Brüx. “Microstructures and Mechanical Properties of High-Strength Fe-Mn-Al-c ...” Steels for Automotive Application, 2016.
76. Howell, Ryan A, and David C Van Aken. “A Literature Review of Age Hardening Fe-Mn-Al-C Alloys.” MATERIALS SCIENCE AND ENGINEERING FACULTY RESEARCH & CREATIVE WORKS, 2009.
77. Bartlett, Laura, and David Van Aken. “High Manganese and Aluminum Steels for the Military and Transportation Industry - Jom.” SpringerLink, Springer US, 2 Aug. 2014.
78. Lee, Keunho, et al. “Effect of Aging Treatment on Microstructure and Intrinsic Mechanical Behavior of Fe–31.4mn–11.4al–0.89c Lightweight Steel.” Journal of Alloys and Compounds, Elsevier, 9 Oct. 2015.
79. Lee, Keunho, et al. “Β-MN Formation and Aging Effect on the Fracture Behavior of High-Mn Low-Density Steels.” Scripta Materialia, Pergamon, 20 July 2016.

80. Wang, Pengjie, et al. “Effect of Secondary Twins on Strain Hardening Behavior of a High Manganese Austenitic Steel at 77 K by Quasi in Situ EBSD.” Materials Characterization, Elsevier, 2 Sept. 2021.
81. Beladi, H., et al. “Orientation Dependence of Twinning and Strain Hardening Behaviour of a High Manganese Twinning Induced Plasticity Steel with Polycrystalline Structure.” Acta Materialia, Pergamon, 20 Oct. 2011.
82. Jacob, Roshan, et al. “Recent Advancements in Manganese Steels – a Review.” Materials Today: Proceedings, Elsevier, 28 Feb. 2020.
83. Haase, Christian, et al. “Applying the Texture Analysis for Optimizing Thermomechanical Treatment of High Manganese Twinning-Induced Plasticity Steel.” Acta Materialia, Pergamon, 3 Sept. 2014.
84. Jeong, J.S., et al. “In Situ Neutron Diffraction Study of the Microstructure and Tensile Deformation Behavior in Al-Added High Manganese Austenitic Steels.” Acta Materialia, Pergamon, 1 Mar. 2012.
85. Tang, Lei, et al. “Synergistic Deformation Pathways in a TWIP Steel at Cryogenic Temperatures: In Situ Neutron Diffraction.” Acta Materialia, Pergamon, 28 Sept. 2020.
86. Kalsar, Rajib, and Satyam Suwas. “A Novel Way to Enhance the Strength of Twinning Induced Plasticity (TWIP) Steels.” Scripta Materialia, Pergamon, 9 June 2018.
87. Chen, Y., et al. “Cumulative Contribution of Grain Structure and Twin Boundaries on Cyclic Deformation Behavior of a 20mn-0.6c- TWIP Steel: Experimental and Theoretical Analysis.” Materials Science and Engineering: A, Elsevier, 11 Sept. 2019.

88. Howell, R., et al. “Tensile, High Strain Rate Compression and Microstructural Evaluation of Lightweight Age Hardenable Cast Fe-30Mn-9al-Xsi-0.9C-0.5Mo Steel - International Journal of Metalcasting.” SpringerLink, Springer International Publishing, 25 Nov. 2015.
89. Li, K., et al. “Strain Rate Dependence on the Evolution of Microstructure and Deformation Mechanism during Nanoscale Deformation in Low Carbon-High MN Twip Steel.” Materials Science and Engineering: A, Elsevier, 2 Nov. 2018.

VITA

Jaehyun Kim earned his bachelor's degree in Metallurgical & Materials Engineering from the University of Texas at El Paso (UTEP), Tx, US in 2020. After his bachelor's degree, he joined the Department of Metallurgical, Materials and Biomedical Engineering at the University of Texas at El Paso to pursue his master's degree in Material Science and Engineering.

Contact Information: jkim10@miners.utep.edu